Ultrasonics 145 (2025) 107492

Contents lists available at ScienceDirect

Ultrasonics

journal homepage: www.elsevier.com/locate/ultras

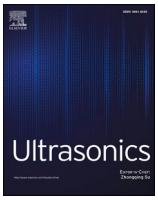

Defect localization in plate structures using the geometric phase of Lamb waves

Guangdong Zhang [a,b], Tribikram Kundu [a,b,c,d,*], Pierre A. Deymier [a,d], Keith Runge [a,d]

[a] New Frontiers of Sound Science and Technology Center, University of Arizona, Tucson, AZ 85721, USA
[b] Department of Aerospace and Mechanical Engineering, University of Arizona, Tucson, AZ 85721, USA
[c] Department of Civil and Architectural Engineering and Mechanics, University of Arizona, Tucson, AZ 85721, USA
[d] Department of Materials Science and Engineering, University of Arizona, Tucson, AZ 85721, USA

ARTICLE INFO

Keywords:
Defect localization
Topological acoustic sensing
Geometric phase change – index (GPC-I)
Lamb waves
Structural health monitoring

ABSTRACT

Commonly used methods for defect localization in structures are based on velocity differences (VD) or amplitude ratio (AR) (or attenuation due to scattering) measured along different sensing paths between a reference system and a defective system. A high value on a sensing path indicates a higher probability of the presence of defect on that path. We introduce an alternative approach based on the newly developed topological acoustic (TA) sensing technique for localizing defects in plate structures using Lamb waves. TA sensing exploits changes in geometric phase of acoustic waves to detect perturbations in the supporting medium. This approach uses a geometric phase change – index (GPC-I), a measure of the geometry of the acoustic field averaged over a spectral domain, as detection metric in lieu of VD or AR. Calculations based on the finite element method (FEM) in Abaqus/CAE software verifies the effectiveness of the proposed GPC-I-based defect localization method. Randomly located defects on the surface of a plate are localized with higher sensitivity and accuracy, by the GPC-I method in comparison to VD or AR-based methods.

1. Introduction

Defects or damages can occur in large-scale engineering structures, such as plate structures, due to foreign object impacts, local erosion, and manufacturing flaws, which can endanger the safety of structural components during operation [1–3]. Localizing these defects or damages is essential to ensure the safe operations of the structures [4]. Ultrasonic nondestructive evaluation (UNDE) techniques are widely used for engineering structural health monitoring (SHM) [5,6]. In particular, ultrasonic Lamb waves have garnered significant attention due to their promising capabilities for long-distance propagation and wide-range sensing coverage [7,8], making them suitable for sensing in large-scale structures. Consequently, developing a sensitive and stable defect localization method based on Lamb waves remains highly desirable for SHM applications.

For localizing defects or damages in engineering structures, most research focused on predicting the acoustic sources generated by the defects. It is done by the popular passive acoustic emission (AE) technique and is commonly known as the acoustic source localization (ASL) [9]. Many researchers investigated the ASL technique and have proposed many ASL methods and algorithms that are suitable in different scenarios [10–15]. Passive AE technique is good for locating the damage initiation point but not for localizing and characterizing existing damages. Also, an already existing damage cannot be localized by the passive AE technique. Therefore, active defect localization method is needed to compensate for the limitations arising from passive ASL techniques. Unlike the vast majority of investigations on ASL technique, only a limited number of investigations have been reported on active defect localization methods in engineering structures. Ma et al. [16] proposed a wave front shape-based method on time-difference-of-arrivals (TDOAs) for active damage localization in composite plates, and this wave front shape based method is an advanced tool adopted in ASL technique without knowing materials' velocity profile. Shu et al. [17] refined the popular conventional time-reversal method (TRM) for damage localization using Lamb waves. In the TRM as well as in its modified version, though reference signal and prior information is not necessary to extract damage features [18–20], the time of arrival (TOA) at the sensors is needed and the time difference of arrival (TDOA) at different sensors is used to identify the damage locations. Other defect localization methods using Lamb waves include analyzing envelope of

* Corresponding author at: New Frontiers of Sound Science and Technology Center, University of Arizona, Tucson, AZ 85721, USA.
E-mail address: tkundu@arizona.edu (T. Kundu).

https://doi.org/10.1016/j.ultras.2024.107492
Received 25 July 2024; Received in revised form 16 October 2024; Accepted 17 October 2024
Available online 19 October 2024

wave modes characteristics [21–23], identical-group-velocity of different wave modes [24] and combining these conventional TOA or envelope feature information with deep learning using neural network [25–27]. The beamforming technique, based on the delay-and-sum principle, is another well-established approach [28,29]. It can be employed for active damage sensing in structures, where the wave beams must be carefully controlled with proper weights to achieve specific sensing objectives [30]. Moreover, beamforming-based techniques can be computationally intensive, as monitoring the entire structure is typically required for accurately localizing potential damage sites [15].

In general, defect localization using ultrasonic Lamb waves basically relies on the accurate determination of TOA to calculate TDOA between undamaged and damaged structures [31,32]. It means that clear Lamb wave modes are required for accurate estimations of time of flight (TOF) or TDOA. However, damage index (DI) based acoustic parameters such as correlation coefficients [33,34], energy ratio or amplitude ratio [35], linear attenuation coefficients [36–38], and nonlinear acoustic parameters like sideband peak count – index (SPC-I) [1–3,5] measures the overall differences between reference signals (healthy structures) and testing signals (damaged structures). Using DIs to characterize damages does not require to track specific Lamb wave modes thus can provide stable damage features. For example, the probability ellipse method with different weights of DIs has been adopted to localize and image damages in structures with active sensors network [39–41]. Hu et al. [42] numerically investigated the detection and localization of a hole type damage in aluminum plate structures using sideband peak count (SPC) based DI.

Recently, another emerging DI called geometric phase change (GPC) based on topological acoustic (TA) sensing has been introduced by some of the authors [43–49]. The GPC quantifies the variation in the geometric phase of an acoustic field (for example, Lamb waves propagating in structures) represented as a state vector in an abstract parameter space – Hilbert space. In the TA sensing technique with GPC, the state of the acoustic field in the unperturbed (damage-free) and perturbed (damaged) cases are mapped as multidimensional vectors in the same Hilbert space. As a global measure of the linear and nonlinear acoustic field a sensing approach based on the geometric phase can have higher sensitivity than magnitude-based or TOF-based sensing approaches.

With the TA sensing technique, originally, changes in complicated environments such as forests [43] or the state of permafrost in the arctic [44] were monitored using seismic waves. This method was further extended to monitoring perturbations due to a mass defect located on an array of coupled acoustic waveguides [45], mass defects in a nonlinear granular metamaterial [46] and a small subwavelength object on a flat surface submerged in water [47]. Taking the advantage of high sensitivity of GPC, Zhang et al. [6,48] successfully investigated damage growth in heterogenous plate structures having complex topography with the GPC parameter. They found that GPC results show superiority in comparison to the SPC-I based technique for monitoring damage evolution in complex heterogeneous structures. A comparative study between GPC-I and SPC-I has been recently carried out and it showed that the GPC-I technique is an effective tool for damage growth monitoring with high sensitivity [49]. However, like other DIs, the GPC can only indicate the existence of defects in the environment or in engineering structures. No attempt has been reported yet on defect localization with the highly sensitive GPC parameter.

In this work, we extend the GPC sensing method to active defect localization for the first time. A geometric phase change – index (GPC-I) derived from GPC spectral averages, serves as a metric for determining the probable location of defects along different sensing paths. Numerical modeling is carried out with finite element method (FEM) in Abaqus/CAE software to verify the effectiveness of the GPC-I localization method. The method is then shown to compare very favorably with similar methods based on more common acoustic parameters, namely – velocity differences based on TOA and signal amplitude or attenuation variations based on recorded signal amplitudes.

2. Theory and methodology

In this section, we briefly review the notions of GPC and GPC – index (GPC-I). A methodology is then introduced for actively locating defects in plate structures.

2.1. Background on GPC plots and GPC-I

The frequency-dependent amplitude of an acoustic field supported by some medium can be represented as a complex vector in an infinite dimensional space whose basis components are associated with every point in the continuous medium. From a practical point of view, one can select a finite dimension subspace by considering the complex amplitude of the field at a discrete subset of "n" points in the medium. The finite set of complex amplitudes forms a complex vector in this n-dimensional subspace. This can be achieved by stimulating the medium at some location and recording the displacement or velocity value as a time series at the "n" chosen receiving locations. Each of these n time series are Fast Fourier Transformed (FFT) to obtain complex amplitudes in the spectral domain. At a given frequency, f, these n complex amplitudes are used to form a normalized n-dimensional state vector. The n basis vectors correspond to the n receiving sensor locations in the physical space. This normalized state vector can be written as [43],

$$C = \frac{1}{\sqrt{C_1^2 + C_2^2 + C_3^2 + \ldots C_n^2}} \begin{pmatrix} C_1 e^{i\phi_1} \\ C_2 e^{i\phi_2} \\ C_3 e^{i\phi_3} \\ \ldots \\ C_n e^{i\phi_n} \end{pmatrix} \tag{1}$$

In equation (1), i is the imaginary unit. C_k and ϕ_k ($k = 1, 2, 3 \ldots n$) are magnitude and spatial phase at each receiving point, respectively. Let us assume that Eq. (1) is representative of a reference medium without any damage. When damages are introduced, the perturbation in the physical space scatters the acoustic waves and modifies the spatial distribution of the acoustic field. The perturbations then change the normalized complex amplitude of the acoustic field to,

$$C' = \frac{1}{\sqrt{C_1'^2 + C_1'^2 + C_1'^2 + \ldots C_n'^2}} \begin{pmatrix} C_1' e^{i\phi_1'} \\ C_2' e^{i\phi_2'} \\ C_3' e^{i\phi_3'} \\ \ldots \\ C_n' e^{i\phi_n'} \end{pmatrix} \tag{2}$$

The angle between the vector representation of the acoustic field along the n locations in the damage-free and damaged systems corresponds to a change in the geometric phase change of the acoustic field associated with the perturbation is then defined as the angle,

$$\Delta\varphi(f) = \arccos(\mathrm{Re}(C^* \bullet C')), \Delta\varphi \in [0, \pi] \tag{3}$$

where C^* denotes the complex conjugate of state vector C while Re stands for the real part of a complex quantity. The GPC, $\Delta\varphi(f)$ measures the effect of the perturbation on the orientation of the field state vector.

The GPC – index (GPC-I) is defined as the average value of $\Delta\varphi(f)$ in some frequency domain. This index provides a metric for quantifying the level of damage of structures with larger damage levels corresponding to larger GPC-I values.

2.2. Defect localization methodology with GPC-I

Consider a damage-free plate structure equipped with multiple sensors distributed across its surface, as depicted in Fig. 1a. Given the practical dimensions of such plates, these sensors are strategically

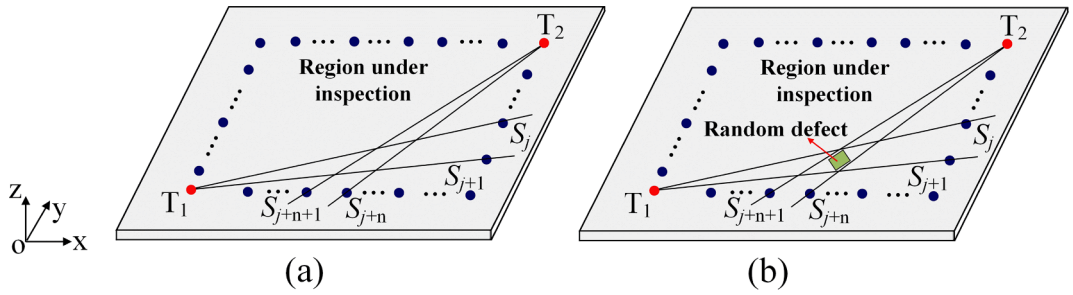

Fig. 1. Schematic illustration of a plate with array of sensors (S_j) for (a) reference plate and (b) perturbed state plate with a random defect.

placed near the plate's edges to encompass a large sensing area (that may or may not have damage). Random defects that require localization may arise within this region due to impacts or local erosion, as shown in Fig. 1b.

We choose the sensor point T_1 as the transmitter. All other sensors record displacement or velocity series generated from T_1. Equations (1) and (2) given in section 2.1 present the general representation of frequency-dependent amplitude of an acoustic field as a complex vector in n dimensional Hilbert space, where equation (1) shows the reference state (undamaged) and equation (2) gives the perturbed state (damaged). For defect localization, the entire region that is under inspection is divided into multiple sub-regions with prescribed receivers, and GPC-I is computed at each receiver one by one. We take two adjacent receivers S_j and S_{j+1} as an example to show how GPC-I is obtained at receiving sensor S_j.

In the reference plate shown in Fig. 1a, since we consider two adjacent receivers (sensors j and $j+1$), a two-dimensional (2-D) complex state vector can be constructed from time series received at these two sensors. From the recorded time series with Fast Fourier Transformation (FFT) we get complex amplitude and phase, the normalized complex state vector at receiving sensor j can be constructed from equation (1) as,

$$C_j = \frac{1}{\sqrt{C_j^2 + C_{j+1}^2}} \begin{pmatrix} C_j e^{i\phi_j} \\ C_{j+1} e^{i\phi_{j+1}} \end{pmatrix} \tag{4}$$

where j denotes the receiving sensor number, and i is the imaginary unit. C and ϕ are magnitude and spatial phase at each receiving point.

Accordingly, in the perturbed plate the normalized 2-D state vector at receiving sensor j can be expressed as,

$$C'_j = \frac{1}{\sqrt{C'^2_j + C'^2_{j+1}}} \begin{pmatrix} C'_j e^{i\phi'_j} \\ C'_{j+1} e^{i\phi'_{j+1}} \end{pmatrix} \tag{5}$$

The GPC at sensor number j is calculated in the 2-D subspace as,

$$\Delta\varphi_j(f) = \arccos\left(\mathrm{Re}\left(C_j^* \bullet C_j'\right)\right), \ \Delta\varphi \in [0, \pi] \tag{6}$$

where C_j^* denotes the complex conjugate of state vector C_j at receiving sensor j while Re stands for the real part of a complex quantity.

It should be noted that equations (4) through (6) give the general form that shows how GPC is obtained at one receiver S_j; GPC at every receiver should be generated following the same process. The GPC-I at the receiving sensor number j is then calculated by averaging $\Delta\varphi_j(f)$ over a chosen frequency range. A large GPC-I value indicates that the presence of a defect is likely along the sensing paths from the transmitter to sensor numbers j and $j+1$. Subsequently, the defect is likely located in the triangular region formed by the transmitter T_1 and the two sensors numbered j and $j+1$. We now consider another transmitter location T_2 and determine the GPC, $\Delta\varphi_{j+n}(f)$, employing the two receiving sensors numbered $j+n$ and $j+n+1$. The value of GPC-I at the receiving sensor $j+n$, is then used to potentially locate the defect in the triangle region formed by T_2, sensors $j+n$ and $j+n+1$. Large values of GPC-I for both triangles predicts the defected region as the intersection of these two triangles. The defective region forms a quadrilateral area whose four vertices are indexed as $k = 1, 2, 3, 4$ with coordinates (x_k, y_k). We define the predicted location (x_p, y_p) of the defect by the following averages:

$$\begin{cases} x_p = \dfrac{\max(x_k) + \min(x_k)}{2} \\ y_p = \dfrac{\max(y_k) + \min(y_k)}{2} \end{cases} \tag{7}$$

3. Numerical model

In this section, numerical modeling analysis is carried out using Abaqus/CAE software. The numerical model includes multiple sensors, numbered from 1 to 32, distributed on the surface of a reference and defective plates. The dimension of both plates (reference and perturbed states) is $300 \times 300 \times 3\text{mm}^3$. The distance between two adjacent receiving points is set at 20 mm. These sensors enclose a square area with a side length of 160 mm as shown in Fig. 2. The defect is formed by attaching one block with dimension $10 \times 10 \times 6\text{mm}^3$ on the surface of the plate structure. The center of the mass defect on the surface in the first quadrant is (50 mm, 30 mm). Then the mass is moved to three additional locations (−20 mm, 20 mm), (−30 mm, −50 mm) and (20 mm, −40 mm). The material properties for the plate structure and the mass defect are the same and are listed in Table 1.

First, we consider sensing paths by defining the sensor number 1 as the transmitter, T_1, and the receiving sensors are 9 to 25. Similarly, we choose sensor 17 as the transmitter T_2. In this case the signals are recorded at sensors 1 to 9 and 25 to 32. Note that there is no constraint on the selection of transmitters and receivers.

A Hanning window modulated excitation field of central frequency 200 kHz with two cycles is applied in the negative z direction, first at $T_1 = 1$, and then at $T_2 = 17$. At the selected receiving points, the out-of-

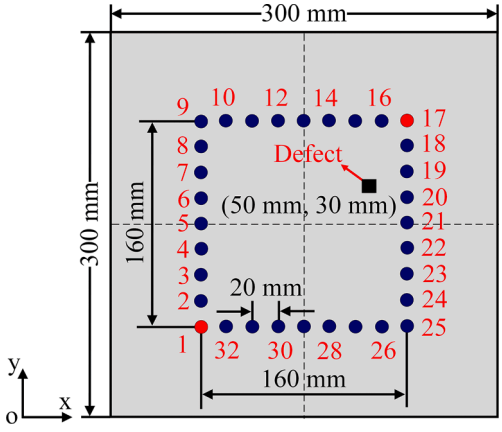

Fig. 2. 2-D view of the problem geometry for numerical modeling – perturbed state with a random defect. The defect is absent in the reference state.

Table 1
Material property parameters of plate structures and mass defects for FEM modeling.

Parameter	Young's modulus (GPa)	Poisson's ratio	Density (kg/m^3)
Values	71.50	0.33	2700.00

plane velocity (in the z direction) is recorded for both the reference state and the perturbed state. The sampling frequency for recording the signals is 50 MSa/s (mega samples per second).

4. Defect localization using GPC-I method

We initially investigate the model system with the defect in the first quadrant of the plate, that is coordinates (50 mm, 30 mm). Fig. 3 shows snapshots of Lamb wave displacement magnitude for both transmitter locations $T_1 = 1$ and $T_2 = 17$.

In Fig. 4, we illustrate the time histories in both reference and perturbed states recorded along two sensing paths defined by the sensor pair 18 and 19 and the sensor pair 23 and 24 when the transmitter is at location $T_1 = 1$.

We note that the first dominant wave packet in Fig. 4 is a A_0 mode while the S_0 wave packet is very weak. In Fig. 5, we show the calculated GPC as a function of frequency for two different sensing paths.

The frequency-dependent GPC plots measure the effect of the perturbation on the acoustic field. Over a wide frequency range (from 0 to 800 kHz) the GPC show significantly larger values at receiving sensor 18 than that at sensor 23. This difference indicates that a defect is more likely to be present along the wave path between the transmitter 1 and sensor 18. The GPC-I is calculated by averaging the GPC over the frequency range 0 to 800 kHz. With the transmitter at location 1, the GPC-I as a function of the sensing path is shown in Fig. 6.

Fig. 6b shows that the defect is more likely to be located within the triangular region enclosed by the transmitter $T_1 = 1$ and the sensors 18 and 19. For the second transmitter location ($T_2 = 17$), GPC-I value at each receiving sensor is obtained and shown in Fig. 7a and the predicted triangular region is shown in Fig. 7b.

Fig. 7b shows that the defect is more likely to be located within the triangular region enclosed by the transmitter $T_2 = 17$ and the sensors 28 and 29. The intersection region between the two triangles with highest GPC-I in Fig. 8 indicates the most probable location of the defect.

This localization process is applied to all defect positions. We list the localization results for other three defect locations in the Appendix. Table 2 summarizes the predictions of the GPC-I localization method for all four defective plates investigated.

Furthermore, a defect localization error analysis is conducted by comparing the predicted location with the actual location. Since the mass defect has some dimensions, the scattered waves received by sensors are affected by the edges of the defect. If we can predict any boundary of the defect then it will be assumed that the localization of this defect is accurately determined. The relative error between the actual and the predicted locations of the defect is defined by equations (8) and (9). Equation (8) indicates that when the predicted location is inside the defect then we say it has accurately localized the defect and the relative error is defined as zero. Otherwise, we use equation (9) to find the values from the predicted location to one of the nearest edges of the defect to calculate the error values.

$$\varepsilon_{GPC-I} = 0, \text{ for } \begin{cases} x_a - \frac{L_{bx}}{2} \le x_p \le x_a + \frac{L_{bx}}{2} \\ y_a - \frac{L_{by}}{2} \le y_p \le y_a + \frac{L_{by}}{2} \end{cases} \tag{8}$$

In equation (8), (x_p, y_p) is the predicted localization coordinate obtained from equation (7). (x_a, y_a) is the actual center location of the defect. L_{bx} and L_{by} are the side lengths of the mass defect in x and y directions, respectively.

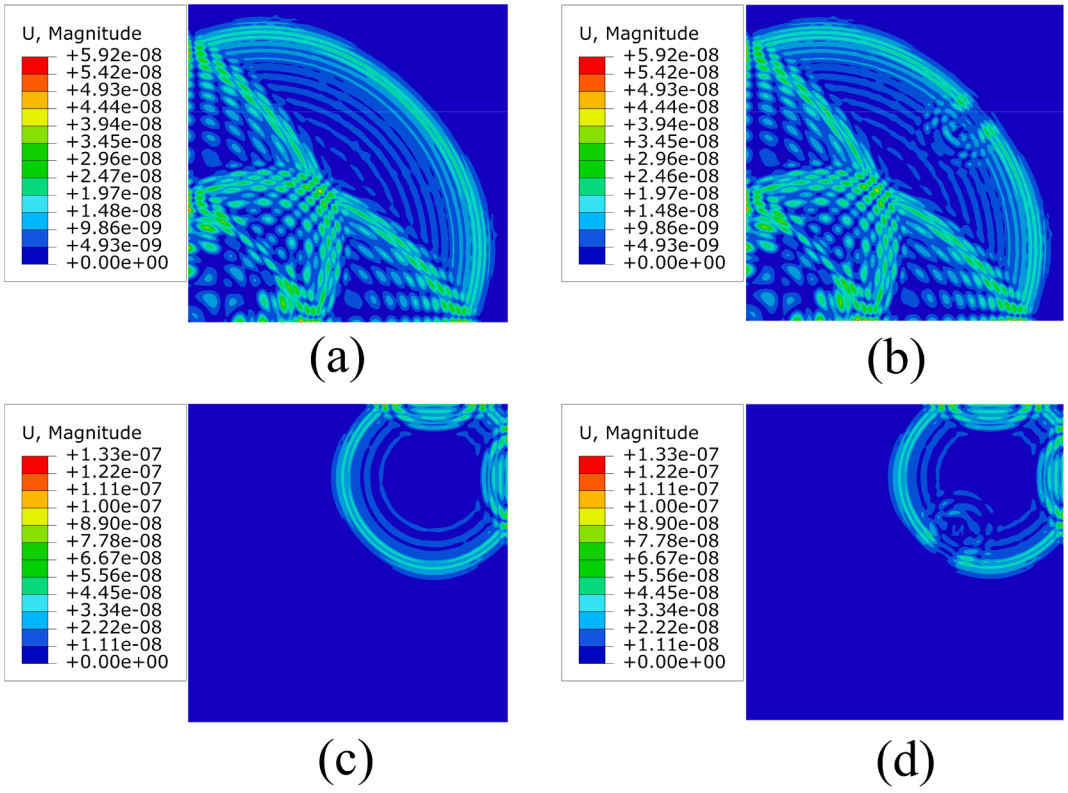

Fig. 3. Lamb wave displacement magnitudes for the reference plate (left column) and defective plate (right column) with transmitter $T_1 = 1$ at time 75 μs (top row) and $T_2 = 17$ at time 35 μs (bottom row). We only show the plate with the defect located in its first quadrant (unit is mm).

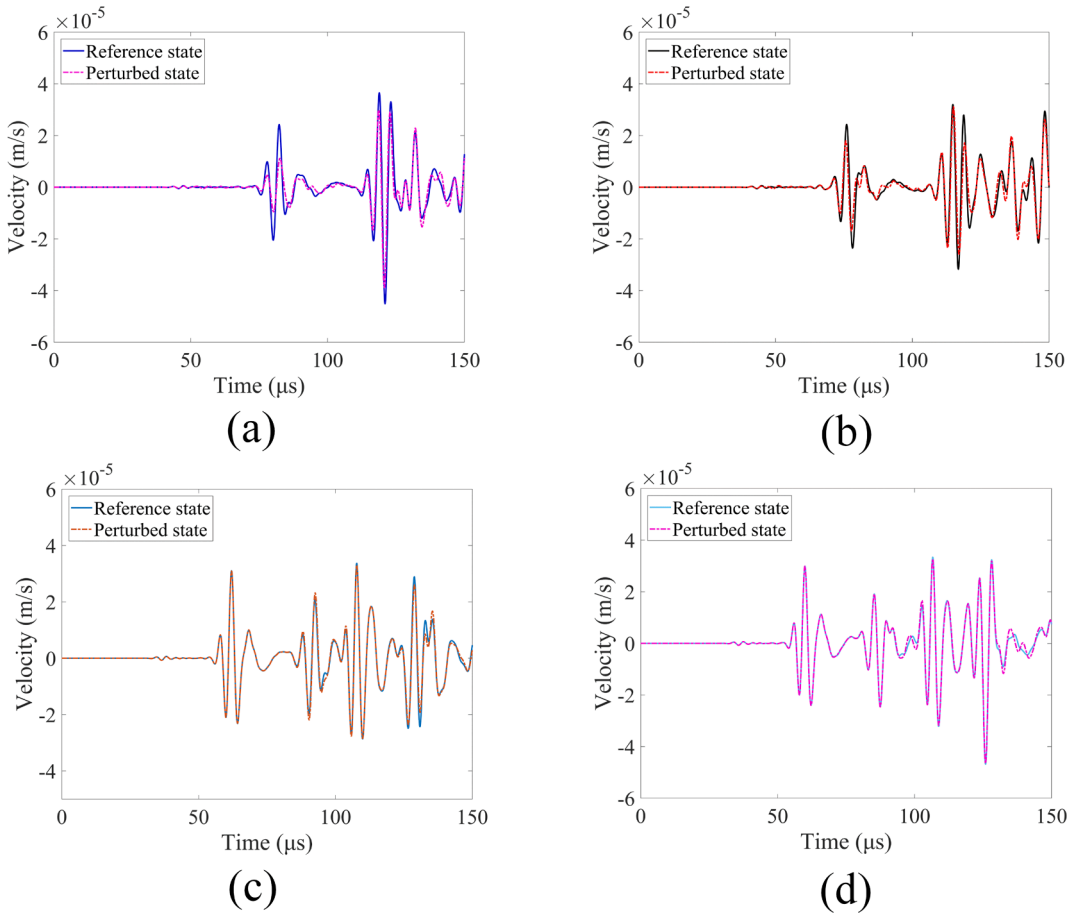

Fig. 4. Time histories for both reference and perturbed states at receiving sensor pair (a) 18, (b) 19, and sensor pair (c) 23 and (d) 24 when the transmitter is at location $T_1 = 1$.

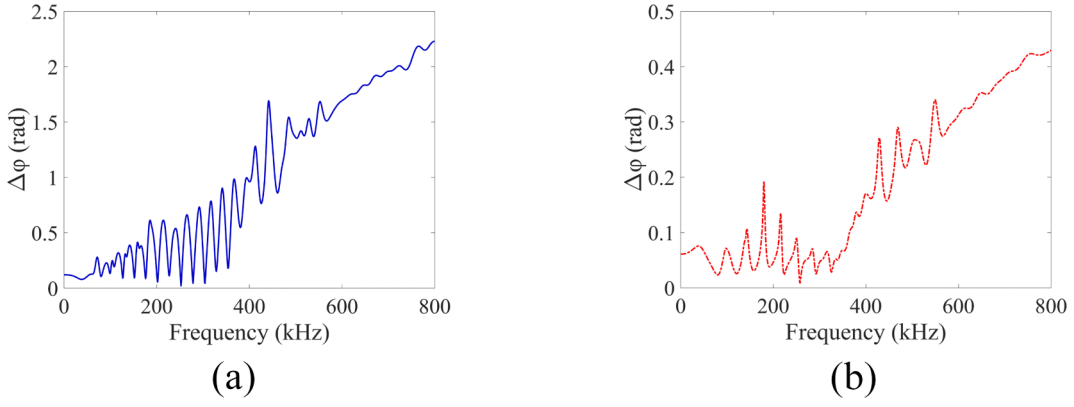

Fig. 5. Calculated GPC for two sensing paths defined by sensor locations (a) 18 and (b) 23 when the transmitter, T_1, is at location 1.

$$\varepsilon_{GPC-I} = \sqrt{\left(\frac{\min\left\{\left|x_p - \left(x_a \pm \frac{L_{bx}}{2}\right)\right|\right\}}{Lx}\right)^2 + \left(\frac{\min\left\{\left|y_p - \left(y_a \pm \frac{L_{by}}{2}\right)\right|\right\}}{Ly}\right)^2} \times 100\% \tag{9}$$

In equation (9), L_x and L_y are side lengths in x and y directions, respectively of the enclosed region by those distributed sensors. The relative error is decomposed into the x and y directions, respectively, and then added to consider their combined effects. The relative errors are small, less than 3 %. It is also interesting to see that for the predicted locations corresponding to defects No. 1 and 3, x and y values and their signs have been simply interchanged. This is because the transmitting sensors 1 and 17 here are symmetric about a diagonal line passing through sensors 9 and 25. All receiving sensors as well as the actual defect locations are also symmetric about this line. Hence, the prediction comes out to be symmetric about this line as well.

5. Effect of number of sensors on defect localization with GPC-I

In section 4, a total of 32 sensors have been adopted for defect

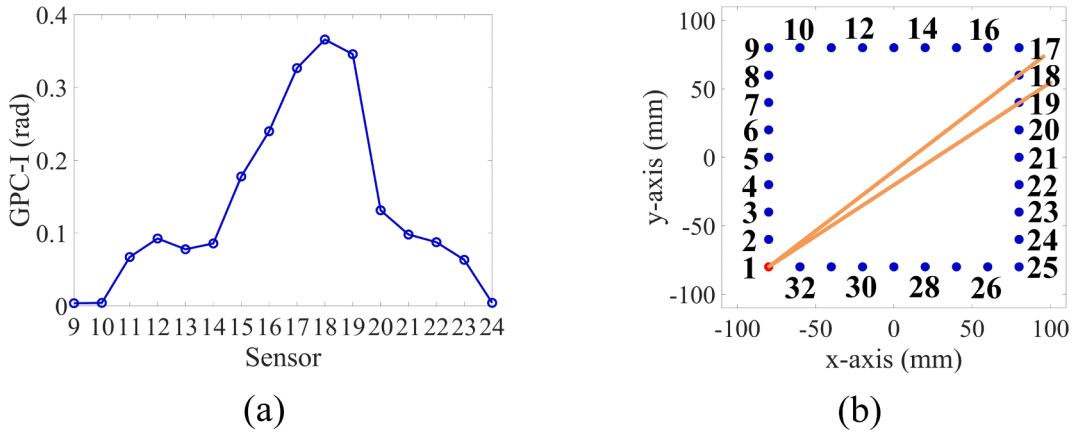

Fig. 6. (a) GPC-I calculated for all sensing paths (labelled by sensor number) with $T_1 = 1$ and (b) the triangular region with maximum GPC-I value.

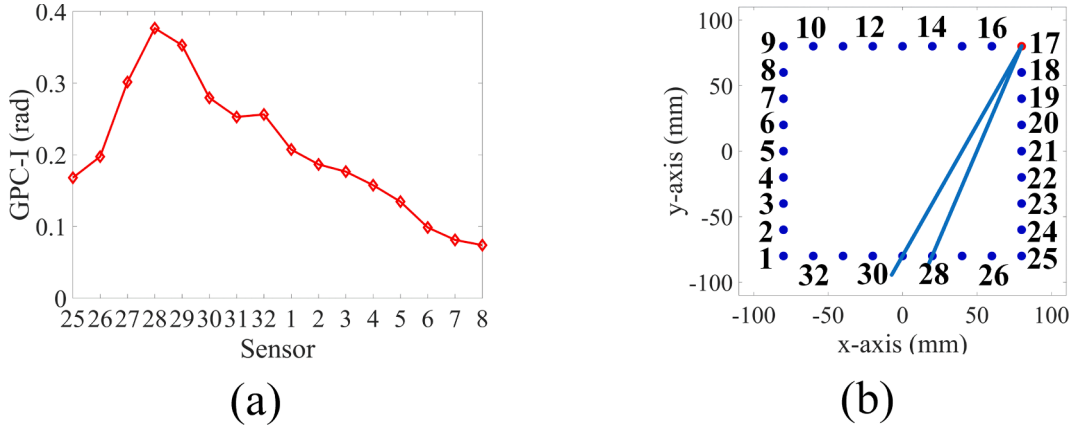

Fig. 7. (a) Same as Fig. 6 but with transmitter T_2 at location 17.

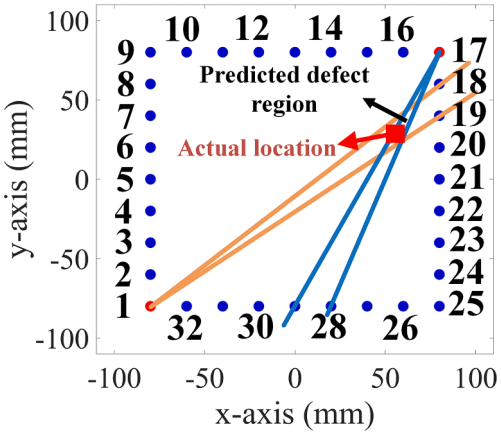

Fig. 8. Predicted defect location in the quadrilateral area formed by the intersection of the two triangles with highest GPC-I.

localization. This arrangement can predict defects with relatively high accuracy. In general, more sensors should enhance the resolution and accuracy of the localization results. However, in practical applications, there should be a balance between the number of sensors and the desired accuracy. In this section, the effects of the number of sensors on the proposed localization method with GPC-I are examined. The 2-D view of the problem geometry for smaller number of sensors is shown in Fig. 9. Here, we only take the defect located in the first quadrant [(50 mm, 30 mm)] as an example to examine the effects of sensor numbers on localization results.

Table 2
Defect localization results based on the proposed GPC-I method and error analysis.

Defect No.	Actual location (x_a, y_a) (mm)	Predicted location (x_p, y_p) (mm)	Relative errors (%)
1	(50 ± 5, 30 ± 5)	(58.42, 33.12)	2.44
2	(−20 ± 5, 20 ± 5)	(−21.82, 21.82)	0
3	(−30 ± 5, −50 ± 5)	(−33.12, −58.42)	2.44
4	(20 ± 5, −40 ± 5)	(12.52, −38.64)	2.75

In Fig. 9, the plate dimensions and other configurations, such as material properties and wave propagation modeling, remain same as those in Fig. 2. The only difference is that in Fig. 9a, the number of sensors is reduced to 16, while in Fig. 9b, this number is further reduced to 8. The distance between adjacent sensors is 40 mm in Fig. 9a and 80 mm in Fig. 9b. Using the same localization process, the defect localization results for these two scenarios are presented in Fig. 10.

As the number of sensors decreases, the predicted defect region (overlapped areas shown in Fig. 10c and 10f) expands. A larger predicted region suggests increasing uncertainty regarding the actual defect's location within this area. Such an increase in uncertainty can lead to misjudgment of the actual defect position. Table 3 presents the error analysis results for defect localization with these two fewer sensor configurations.

It can be observed that when the number of sensors decreases from 32 to 16 (as seen in Figs. 2 and 9a), the relative error increases from 2.44 % to 9.88 % −approximately a fourfold rise. This is expected, as a

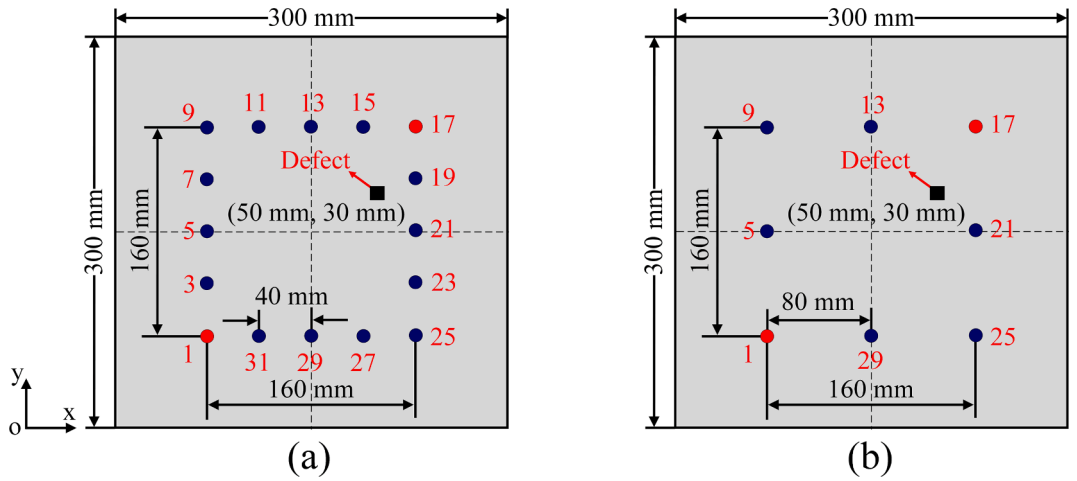

Fig. 9. 2-D view of the problem geometry for numerical modeling for the perturbed state with a random defect for a smaller number of sensors. (a) 16 sensors and (b) 8 sensors. The defect is absent in the reference state.

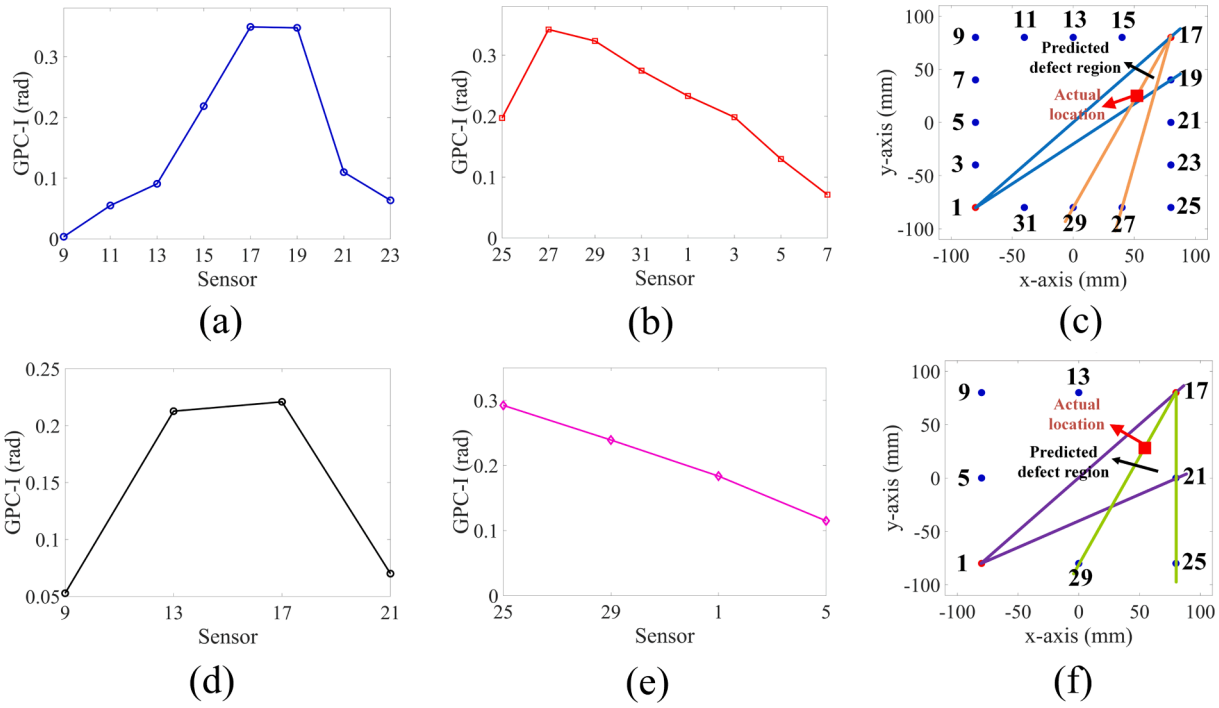

Fig. 10. Defect localization results using transmitters located at positions 1 and 17 for the actual defect positioned at (50 mm, 30 mm). Subplots (a) and (d) show GPC-I results for transmitter 1, while (b) and (e) display GPC-I results for transmitter 17. Subplots (c) and (f) illustrate the predicted defect regions (common areas of the two large triangles) and actual defect location. The top row uses 16 sensors, whereas the bottom row utilizes 8 sensors.

Table 3
Defect localization results based on the proposed GPC-I method and error analysis for fewer number of sensors.

Number of sensors	Actual location (x_a, y_a) (mm)	Predicted location (x_p, y_p) (mm)	Relative errors (%)
16	(50 ± 5, 30 ± 5)	(64, 48)	9.88
8	(50 ± 5, 30 ± 5)	(53.33, 26.67)	0

sparser sensor array reduces the spatial resolution for defect localization. However, when the number of sensors is further reduced to 8, the relative error shows an outlier value of "0" indicating perfect prediction. It is important to note that this accuracy does not imply that fewer sensors are advantageous for defect localization. On the contrary, this result suggests the adverse effects of random predictions due to insufficient sensor density. The outlier of "0" occurs simply because, in this case, the actual location coincidentally aligns with the predicted one. As illustrated in Fig. 10f, the predicted region is bigger, allowing the actual location to fall anywhere within it (almost randomly) making the prediction error relatively small, however the uncertainty associated with this prediction is higer. Future work will focus on optimizing our proposed method by determining the optimal number of sensors and further evaluating its accuracy in defect localization, providing more specific and scientifically robust insights.

6. Comparison between GPC-I localization method and other methods

6.1. Localization based on velocity differences

In this section, velocity differences (VD) between reference state and perturbed state at each receiving sensor are obtained from the time of arrival (TOA) or time of flight (TOF) measurements. The VD parameter is then used to localize the defect following the same steps described above but GPC-I values are replaced by VD values. For the VD calculation from the TOF values, the distances from transmitter 1 to all receiving sensors are first calculated and shown in Fig. 11a. Time histories showing the S_0 mode arrivals at sensor locations 18 and 23 in reference state and perturbed state are shown in Fig. 11b and 11c, respectively.

First, the velocity value at each receiving sensor is calculated for both the reference state and the perturbed state. Then these velocity values are normalized with respect to the first velocity value (received at the first sensor, for transmitter at location 1 and the receiver at location 9) in each state (reference and perturbed). After taking the differences between the normalized velocity values of reference state and perturbed state the GPC-I values are replaced by the VD values for the damage localization. The normalized VD results from transmitter 1 at each receiving sensor are shown in Fig. 12a. It can be seen that there are three peaks (sharp peaks indicate defects appearing on the corresponding path) in the normalized VD plot which makes it difficult to determine the path along which defects occur. However, here we choose the peak with the largest magnitude as the indictor. Then the defect occurs on the path connecting transmitter 1 and sensor 19. Similarly, when transmitter at location 17 is the emitter, the largest peak appears at sensor 27 (shown in Fig. 12b). Then the predicted defect location is determined as the intersection of these two lines obtained from transmitters 1 and 17 as shown in Fig. 12c.

Following the same methodology and using the VD values, defects located for other three positions of the extra mass are shown in Fig. 13.

Defect localization results using velocity differences are summarized in Table 4. The error is calculated using the same equations presented in section 4.

It can be seen in these localization results that for some defect locations (defects 2 and 4) there are large deviations between the predicted defect location and its actual location (shown in Fig. 13a and 13c). Therefore, we can say that the VD parameter is unstable for defect localization.

6.2. Localization based on amplitude ratio

In this section, the amplitude ratio (AR) parameter is utilized to localize the defect for comparison. The AR value at each receiving sensor is defined as the ratio between the maximum peak value in spectral amplitude plots between the reference state and the perturbed state. Spectral amplitude plots at receiving sensors 18 and 23 for both the reference state and the perturbed state are presented in Fig. 14a and 14b, respectively, as an example.

The amplitude ratio at each receiving sensor is calculated and used to localize the defect. The amplitude ratio results for transmitter 1 at each receiving sensor are shown in Fig. 15a. It can be seen that there is a sharp dip at receiving sensor 18 and multiple small peaks and dips (oscillations) at other sensors. Here we choose the largest deviation of a peak or a dip value as the indictor that defects appear on the sensing path which is from transmitter 1 to receiving sensor 18. Similarly, when the transmitter is at location 17 the largest deviation appears at receiving sensor 32 (shown in Fig. 15b). Then the predicted defect location is determined as the intersection of these two lines going through transmitters 1 and 17 as shown in Fig. 15c.

Defect localization results using AR parameter for other positions of the defect are shown in Fig. 16. These defect localization results are summarized in Table 5.

It can be seen in these localization results that for some defects (defects 1, 3 and 4) there are large deviations between predicted defect location and actual location (shown in Fig. 15c, 16b and 16c). The relative errors varied from less than 2 % to more than 30 %; therefore, the AR parameter is also not reliable for defect localization.

7. Discussions and conclusions

This investigation is performed using Abaqus/CAE simulation software. In numerical modeling investigations without any background noise, defect locations can be predicted in some cases (defects 1 and 3) with the VD parameter. However, in real life structural health monitoring (SHM) applications with high background noise, obtaining accurate time of flight (TOF) estimations can become nearly impossible. GPC or GPC-I, on the other hand, exhibit stable and clear damage features with high sensitivity. The GPC-I-based method, introduced here, demonstrates superior accuracy in locating defects on plates compared to the more commonly used approaches based on the wave velocity or the amplitude difference. The velocity differences show very low sensitivity (< 2 % difference in velocity) between reference and perturbed states. Such small difference can be recorded through numerical modeling but can be difficult to detect experimentally or for in situ applications. The amplitude ratio parameter exhibits higher sensitivity to defects than velocity difference. However, amplitude ratio finds difficulty in identifying paths most likely to contain defects due to strong spatial variations.

The GPC-I is a global measure of the acoustic field which does not require precise TOF or time-difference-of-arrival (TDOA) information, nor any specific Lamb wave modes. Consequently, the GPC-I method

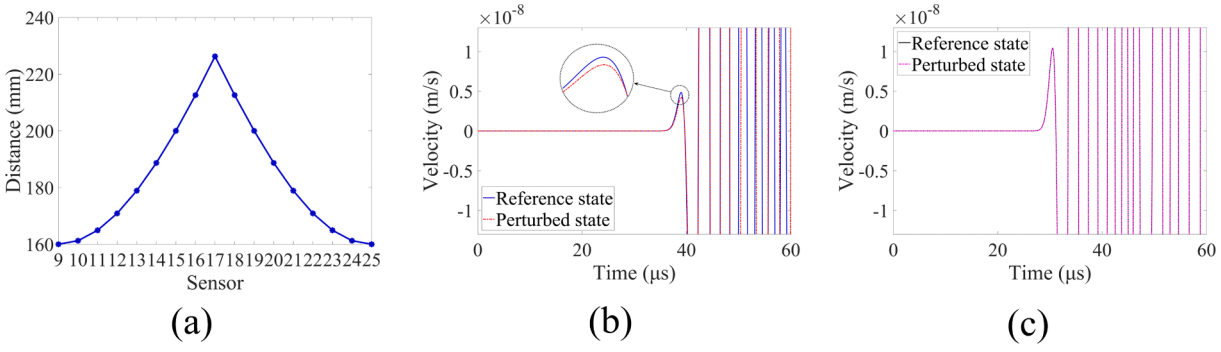

Fig. 11. (a) Distances from the transmitter 1 to all receiving sensors, (b) time histories recorded at sensor 18 for the reference state (defect-free) and the perturbed state (with defect) and (c) time histories recorded at sensor 23 for the reference state and the perturbed state.

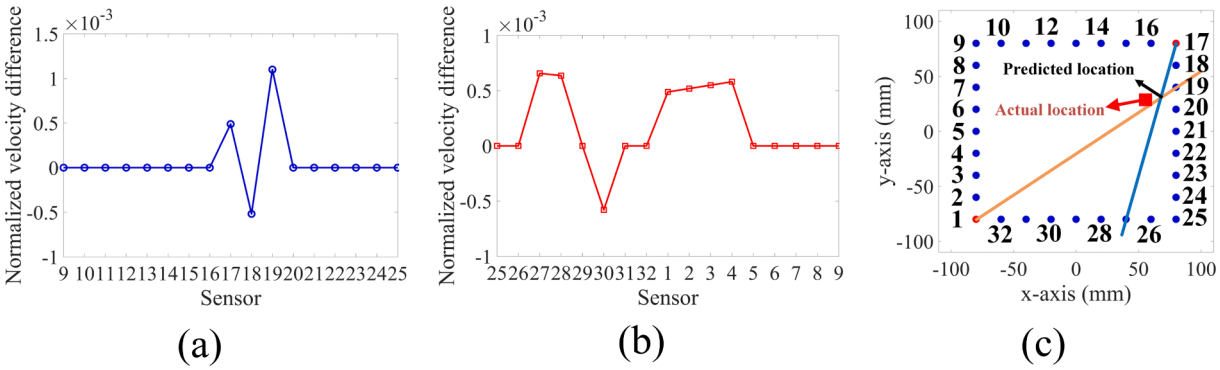

Fig. 12. Defect localization results from transmitters 1 and 17 when the actual mass is located at coordinate (50 mm, 30 mm) (a) normalized velocity differences resulted from transmitter 1 (b) normalized velocity differences resulted from transmitter 17, (c) predicted defect location and actual defect location.

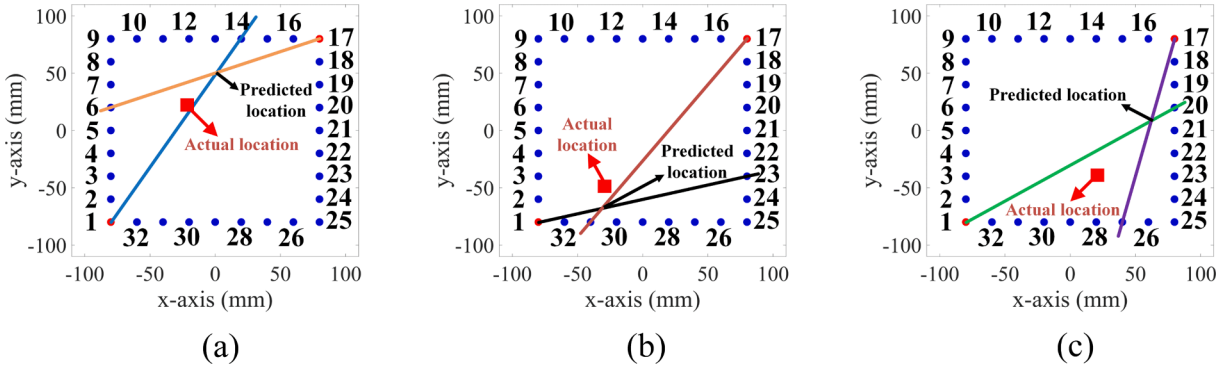

Fig. 13. VD based localization results for defect locations (a) (−20 mm, 20 mm), (b) (−30 mm, −50 mm) and (c) (20 mm, −40 mm).

Table 4
Defect localization results and relative errors obtained from the analysis using velocity differences.

Defect No.	Actual location (x_a, y_a) (mm)	Predicted location (x_p, y_p) (mm)	Relative errors (%)
1	(50 ± 5, 30 ± 5)	(67.69, 30.77)	8.36
2	(−20 ± 5, 20 ± 5)	(1.63, 50.61)	19.09
3	(−30 ± 5, −50 ± 5)	(−30.77, −67.69)	8.36
4	(20 ± 5, −40 ± 5)	(62.22, 8.89)	35.97

holds significant promise for advancing the defect localization technique in large engineering structures, thereby offering substantial benefits to the SHM community. This work is the first attempt to achieve defect localization using the highly sensitive GPC-I parameter. The homogeneous aluminum plate structure provides an ideal medium for evaluating and validating our proposed localization method. However, the advantages of the GPC-I-based sensing method make it particularly well-suited for monitoring damage in more complex structures, such as heterogeneous structures composed of multiple materials and structures with complex topographies [6,48], where defects may be obscured by complex wave interference. Future research will focus on extending the applicability of the proposed method to complex heterogeneous

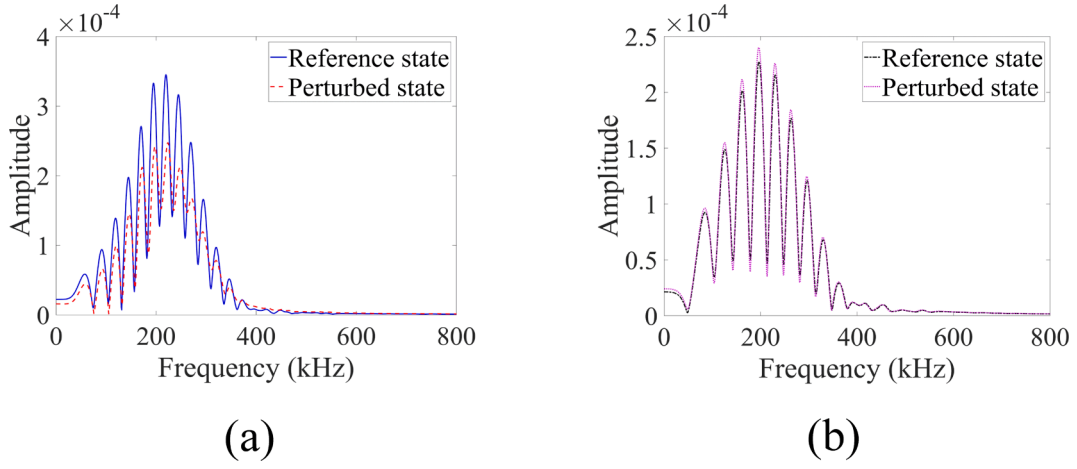

Fig. 14. (a) Spectral amplitude plots for signals recorded at sensor 18 for the reference state and the perturbed state and (b) Spectral amplitude plots for signals recorded at sensor 23 for the reference state and the perturbed state when the transmitter, T_1, is at location 1.

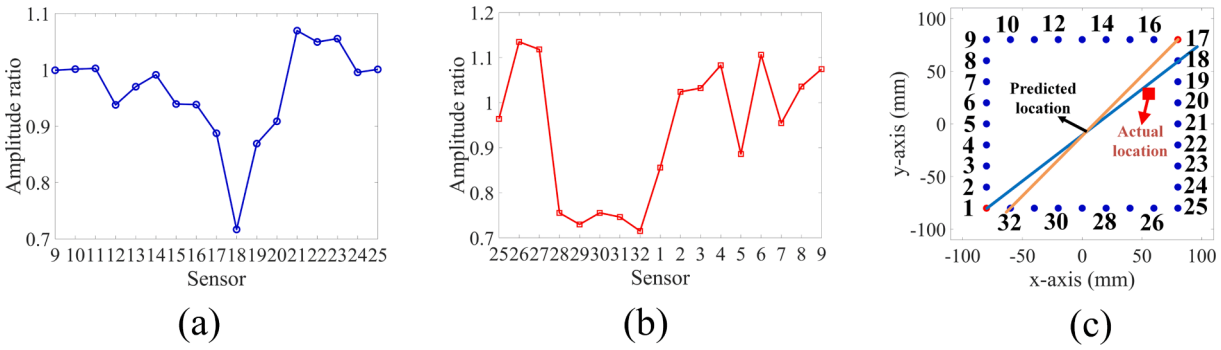

Fig. 15. Defect localization results from transmitters 1 and 17 when the extra mass is located at coordinate (50 mm, 30 mm) (a) amplitude ratio results for transmitter location 1 (b) amplitude ratio results for transmitter location 17, (c) predicted defect location and actual defect location.

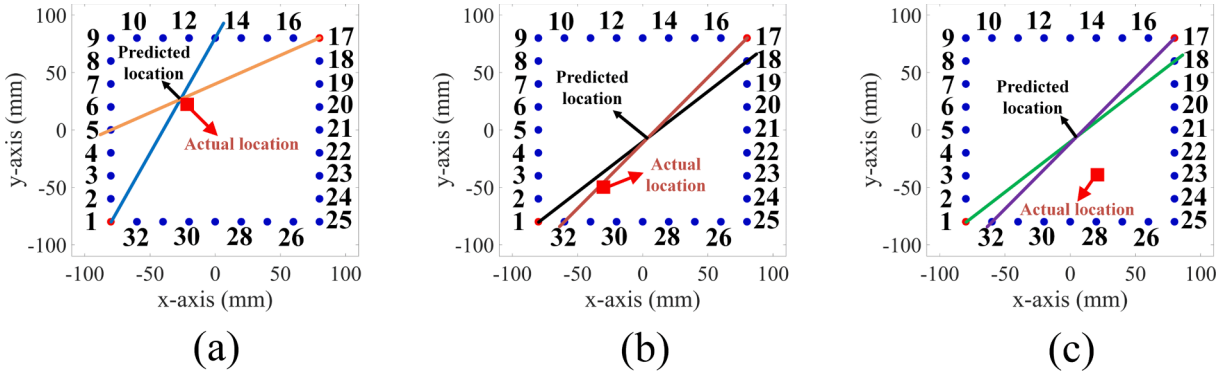

Fig. 16. AR based localization results for defect locations (a) (−20 mm, 20 mm), (b) (−30 mm, −50 mm) and (c) (20 mm, −40 mm).

Table 5
Defect localization results and relative errors obtained from the analysis using amplitude ratio.

Defect No.	Actual location (x_a, y_a) (mm)	Predicted location (x_p, y_p) (mm)	Relative errors (%)
1	(50 ± 5, 30 ± 5)	(5.33, −5.33)	31.21
2	(−20 ± 5, 20 ± 5)	(−26.67, 26.67)	1.47
3	(−30 ± 5, −50 ± 5)	(5.33, −5.33)	31.21
4	(20 ± 5, −40 ± 5)	(5.33, −5.33)	19.50

structures with multiple defects for the real-world SHM applications.

CRediT authorship contribution statement

Guangdong Zhang: Writing – original draft, Validation, Software, Methodology, Investigation, Formal analysis, Data curation, Conceptualization. **Tribikram Kundu:** Writing – review & editing, Supervision, Methodology, Investigation, Conceptualization. **Pierre A. Deymier:** Writing – review & editing, Project administration, Investigation, Funding acquisition. **Keith Runge:** Writing – review & editing, Project administration, Investigation.

Declaration of competing interest

The authors declare that they have no known competing financial interests or personal relationships that could have appeared to influence the work reported in this paper.

Acknowledgements

This work was partially supported by the National Science Foundation sponsored "New Frontiers of Sound Science and Technology Center" at the University of Arizona (Grant No. 2242925).

Appendix

Defect localization at other locations using GPC-I.

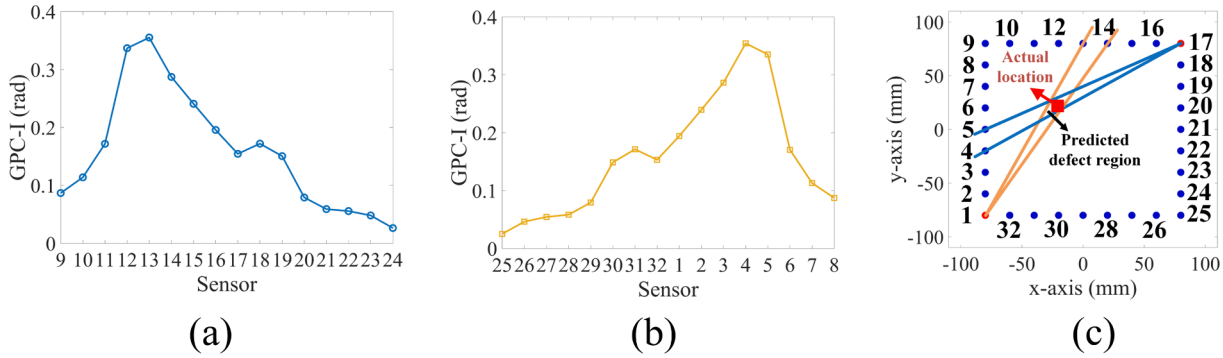

Fig. A1. Defect localization results from transmitters placed at locations 1 and 17 for the actual mass located at (−20 mm, 20 mm) (a) GPC-I results for transmitter 1 (b) GPC-I results for transmitter 17, (c) predicted defect region and the actual defect location.

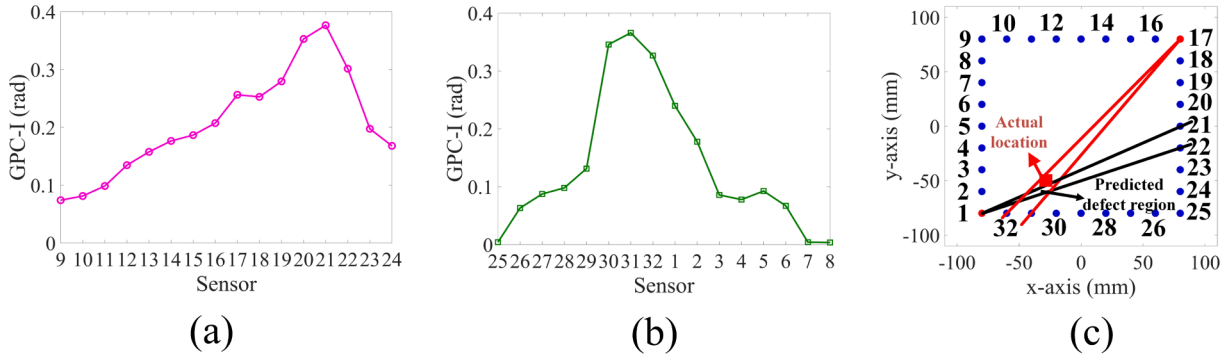

Fig. A2. Defect localization results from transmitters placed at locations 1 and 17 for the actual mass located at (−30 mm, −50 mm) (a) GPC-I results for transmitter 1 (b) GPC-I results for transmitter 17, (c) predicted defect region and the actual defect location.

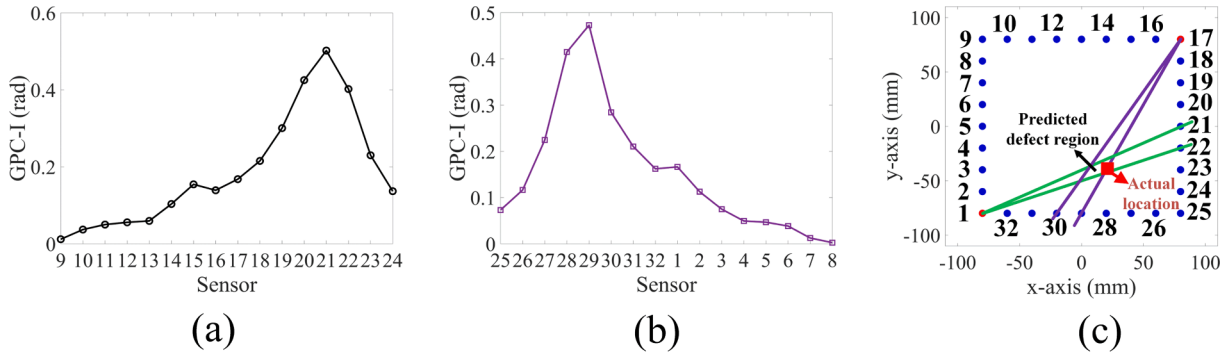

Fig. A3. Defect localization results from transmitters placed at locations 1 and 17 for the actual mass located at (20 mm, −40 mm) (a) GPC-I results for transmitter 1 (b) GPC-I results for transmitter 17, (c) predicted defect region and the actual defect location.

Data availability

Data will be made available on request.

References

[1] G. Zhang, X. Li, S. Zhang, et al., Sideband peak count-index technique for monitoring multiple cracks in plate structures using ordinary state-based peri-ultrasound theory, J. Acoust. Soc. Am. 152 (5) (2022) 3035–3048.
[2] G. Zhang, X. Li, T. Kundu, Ordinary state-based peri-ultrasound modeling to study the effects of multiple cracks on the nonlinear response of plate structures, Ultrasonics 133 (2023) 107028.
[3] G. Zhang, X. Li, T. Li, et al., Ordinary state-based peri-ultrasound modeling for monitoring crack propagation in plate structures using sideband peak count-index technique, J. Sound Vib. 568 (2024) 117962.
[4] C.C. Ciang, J.R. Lee, H.J. Bang, Structural health monitoring for a wind turbine system: a review of damage detection methods, Meas. Sci. Technol. 19 (12) (2008) 122001.
[5] G. Zhang, B. Hu, H. Alnuaimi, et al., Numerical modeling with experimental verification investigating the effect of various nonlinearities on the sideband peak count-index technique, Ultrasonics 138 (2024) 107259.
[6] G. Zhang, P.A. Deymier, K. Runge, et al., Monitoring damage growth and topographical changes in plate structures using sideband peak count-index and topological acoustic sensing techniques, Ultrasonics 141 (2024) 107354.
[7] Q. Ma, G. Tian, Y. Zeng, et al., Pipeline in-line inspection method, instrumentation and data management, Sensors 21 (11) (2021) 3862.
[8] E. El-Shafeiy, M. Alsabaan, M.I. Ibrahem, et al., Real-time anomaly detection for water quality sensor monitoring based on multivariate deep learning technique, Sensors 23 (20) (2023) 8613.
[9] T. Kundu, Acoustic source localization, Ultrasonics 54 (1) (2014) 25–38.
[10] A. Tobias, Acoustic-emission source location in two dimensions by an array of three sensors, Non-Destr. Test. 9 (1) (1976) 9–12.
[11] M. Koabaz, T. Hajzargarbashi, T. Kundu, et al., Locating the acoustic source in an anisotropic plate, Struct. Health Monit. 11 (3) (2012) 315–323.
[12] S. Yin, Z. Cui, T. Kundu, Acoustic source localization in anisotropic plates with "Z" shaped sensor clusters, Ultrasonics 84 (2018) 34–37.
[13] N. Sen, T. Kundu, A new wave front shape-based approach for acoustic source localization in an anisotropic plate without knowing its material properties, Ultrasonics 87 (2018) 20–32.
[14] N. Sen, M. Gawroński, P. Packo, et al., Square-shaped sensor clusters for acoustic source localization in anisotropic plates by wave front shape-based approach, Mech. Syst. Sig. Process. 153 (2021) 107489.
[15] H. Alnuaimi, U. Amjad, T. Kundu, Acoustic source localization in composite plates using Sideband Peak Count-Index technique, Ultrasonics 138 (2024) 107273.

[16] C. Ma, J. Liu, Z. Cui, et al., A damage localization technique using wave front shapes in composite laminates without knowing the velocity profile, Ultrasonics 107357 (2024).
[17] Z. Shu, J. He, M. Hu, et al., Damage location of plate structures based on the exchanging-element time-reversal method by using Lamb waves, J. Sound Vib. 565 (2023) 117907.
[18] R.K. Ing, M. Fink, Self-focusing and time recompression of Lamb waves using a time reversal mirror, Ultrasonics 36 (1–5) (1998) 179–186.
[19] X. Sun, S. Fan, C. Liu, Multitype damage imaging in concrete modeling based on time reversal technique, Buildings 12 (4) (2022) 430.
[20] L. Huang, L. Zeng, J. Lin, et al., An improved time reversal method for diagnostics of composite plates using Lamb waves, Compos. Struct. 190 (2018) 10–19.
[21] Z. Liu, K. Sun, G. Song, et al., Damage localization in aluminum plate with compact rectangular phased piezoelectric transducer array, Mech. Syst. Sig. Process. 70 (2016) 625–636.
[22] A. Ebrahimkhanlou, B. Dubuc, S. Salamone, Damage localization in metallic plate structures using edge-reflected lamb waves, Smart Mater. Struct. 25 (8) (2016) 085035.
[23] D. Stojić, T. Nestorović, N. Marković, et al., Experimental and numerical research on damage localization in plate-like concrete structures using hybrid approach, Struct. Control Health Monit. 25 (9) (2018) e2214.
[24] L. Huang, J. Ding, J. Lin, et al., Detection and localization of corrosion using identical-group-velocity Lamb wave modes, Nondestructive Testing and Evaluation 39 (3) (2024) 594–613.
[25] S. Zhang, C.M. Li, W. Ye, Damage localization in plate-like structures using time-varying feature and one-dimensional convolutional neural network, Mech. Syst. Sig. Process. 147 (2021) 107107.
[26] M. Rautela, S. Gopalakrishnan, Ultrasonic guided wave based structural damage detection and localization using model assisted convolutional and recurrent neural networks, Expert Syst. Appl. 167 (2021) 114189.
[27] Y. Gao, L. Sun, R. Song, et al., Damage localization in composite structures based on Lamb wave and modular artificial neural network, Physical, Sensors and Actuators A, 2024, p. 115644.
[28] H. Nakatani, T. Hajzargarbashi, K. Ito, et al., Locating point of impact on an anisotropic cylindrical surface using acoustic beamforming technique, Key Eng. Mater. 558 (2013) 331–340.
[29] D. Xiao, T. He, Q. Pan, et al., A novel acoustic emission beamforming method with two uniform linear arrays on plate-like structures, Ultrasonics 54 (2) (2014) 737–745.
[30] S. Sundararaman, D.E. Adams, E.J. Rigas, Structural damage identification in homogeneous and heterogeneous structures using beamforming, Struct. Health Monit. 4 (2) (2005) 171–190.
[31] D. Dai, Q. He, Structure damage localization with ultrasonic guided waves based on a time–frequency method, Signal Process. 96 (2014) 21–28.
[32] S. Cantero-Chinchilla, J. Chiachío, M. Chiachío, et al., A robust Bayesian methodology for damage localization in plate-like structures using ultrasonic guided-waves, Mech. Syst. Sig. Process. 122 (2019) 192–205.
[33] Zhao X, Gao H, Zhang G, et al. Active health monitoring of an aircraft wing with embedded piezoelectric sensor/actuator network: I. Defect detection, localization and growth monitoring. Smart materials and structures, 2007, 16(4): 1208.
[34] S. Mustapha, L. Ye, X. Dong, et al., Evaluation of barely visible indentation damage (BVID) in CF/EP sandwich composites using guided wave signals, Mech. Syst. Sig. Process. 76 (2016) 497–517.
[35] J.B. Ihn, F.K. Chang, Pitch-catch active sensing methods in structural health monitoring for aircraft structures, Struct. Health Monit. 7 (1) (2008) 5–19.
[36] H. Sohn, H.W. Park, K.H. Law, et al., Combination of a time reversal process and a consecutiv outlier analysis for baseline-free damage diagnosis, J. Intell. Mater. Syst. Struct. 18 (4) (2007) 335–346.
[37] G. Zhang, X. Liu, X. Li, et al., Measurement of shear wave attenuation coefficient using a contact pulse-echo method with consideration of partial reflection effects, Meas. Sci. Technol. 30 (11) (2019) 115601.
[38] G. Zhang, X. Li, S. Zhang, et al., Investigation of frequency-dependent attenuation coefficients for multiple solids using a reliable pulse-echo ultrasonic measurement technique, Measurement 177 (2021) 109270.
[39] X. Zhao, T. Qian, G. Mei, et al., Active health monitoring of an aircraft wing with an embedded piezoelectric sensor/actuator network: II, Wireless Approaches. Smart Materials and Structures 16 (4) (2007) 1218.
[40] C. Zhou, Z. Su, L. Cheng, Probability-based diagnostic imaging using hybrid features extracted from ultrasonic Lamb wave signals, Smart Mater. Struct. 20 (12) (2011) 125005.
[41] G. Liu, B. Wang, L. Wang, et al., Probability-based diagnostic imaging with corrected weight distribution for damage detection of stiffened composite panel, Struct. Health Monit. 21 (4) (2022) 1432–1446.
[42] B. Hu, T. Kundu, Damage detection and localization in a plate-like structure using sideband peak count (SPC) technique, Ultrasonics 107485 (2024).
[43] T.D. Lata, P.A. Deymier, K. Runge, et al., Topological acoustic sensing of spatial patterns of trees in a model forest landscape, Ecol. Model. 419 (2020) 108964.
[44] T.D. Lata, P.A. Deymier, K. Runge, et al., Topological acoustic sensing of ground stiffness: Presenting a potential means of sensing warming permafrost in a forest, Cold Reg. Sci. Technol. 199 (2022) 103569.
[45] T.D. Lata, P.A. Deymier, K. Runge, et al., Topological acoustic sensing using nonseparable superpositions of acoustic waves, Vibration 5 (3) (2022) 513–529.
[46] M.A. Hasan, P.A. Deymier, Modeling and simulations of a nonlinear granular metamaterial: application to geometric phase-based mass sensing, Model. Simul. Mater. Sci. Eng. 30 (7) (2022) 074002.
[47] T.D. Lata, P.A. Deymier, K. Runge, et al., Underwater acoustic sensing using the geometric phase, J. Acoust. Soc. Am. 154 (5) (2023) 2869–2877.
[48] G. Zhang, B. Hu, H. Alnuaimi, et al., Numerical modeling with experimental verification investigating the effects of nonlinearities on the sideband peak count-index technique and topological acoustic sensing. Health Monitoring of Structural and Biological Systems XVIII, SPIE 12951 (2024) 372–407.
[49] G. Zhang, T. Kundu, P.A. Deymier, K. Runge, A comparative study of geometric phase change- and sideband peak count-based techniques for monitoring damage growth and material nonlinearity, Sensors 24 (2024) 6552.